



# Ultrahigh-resolution optical coherence tomography/angiography with an economic and compact supercontinuum laser

TAI-ANG WANG,<sup>1,6</sup> MING-CHE CHAN,<sup>1,6</sup> HSIANG-CHIEH LEE,<sup>2,3</sup>  
CHENG-YU LEE,<sup>4</sup> AND MENG-TSAN TSAI<sup>4,5,\*</sup> 

<sup>1</sup>*Institute of Photonic System, College of Photonics, National Chiao-Tung University, Tainan City 71150, Taiwan*

<sup>2</sup>*Graduate Institute of Photonics and Optoelectronics, National Taiwan University, 10617, Taiwan*

<sup>3</sup>*Department of Electrical Engineering, National Taiwan University, Taipei 10617, Taiwan*

<sup>4</sup>*Department of Electrical Engineering, Chang Gung University, Taoyuan 33302, Taiwan*

<sup>5</sup>*Department of Neurosurgery, Chang Gung Memorial Hospital, Linkou, Taoyuan 33305, Taiwan*

<sup>6</sup>*The authors contributed equally to this work*

\*[mttsai@mail.cgu.edu.tw](mailto:mttsai@mail.cgu.edu.tw)

**Abstract:** In this study, a Q-switch pumped supercontinuum laser (QS-SCL) is used as a light source for *in vivo* imaging via ultrahigh-resolution optical coherence tomography and angiography (UHR-OCT/OCTA). For this purpose, an OCT system based on a spectral-domain detection scheme is constructed, and a spectrometer with a spectral range of 635 – 875 nm is designed. The effective full-width at half maximum of spectrum covers 150 nm, and the corresponding axial and transverse resolutions are 2 and 10  $\mu\text{m}$  in air, respectively. The relative intensity noise of the QS-SCL and mode-locked SCL is quantitatively compared. Furthermore, a special processing algorithm is developed to eliminate the intrinsic noise of QS-SCL. This work demonstrates that QS-SCLs can effectively reduce the cost and size of UHR-OCT/OCTA instruments, making clinical applications feasible.

© 2019 Optical Society of America under the terms of the [OSA Open Access Publishing Agreement](#)

## 1. Introduction

Optical coherence tomography (OCT) allows acquiring cross-sectional images of biological tissues without the use of fluorescence dyes and contrast agents [1,2]. Based on the interference spectrum generated by the light backscattered from the tissue and that reflected from the reference arm of an interferometer, the depth-resolved biological microstructure can be obtained by conducting the Fourier transform of the interference spectrum known as Fourier-domain OCT (FD-OCT) [3,4]. In contrast to other imaging techniques such as fluorescence microscopy [5] and confocal microscopy [6], OCT utilizes a low-coherence light source without depth scanning to acquire three-dimensional micromorphology of a biological sample. A light source with a broader spectral range could be more suitable for OCT applications because the axial resolution of OCT depends on its center wavelength and bandwidth [7]. Thus, both a coherent light source with a shorter center wavelength and a light source with a broadband spectrum can achieve a higher axial resolution. Moreover, the use of ultrahigh-resolution OCT (UHR-OCT) based on an ultra-broadband light source has been considered for cellular-level imaging [8]. The application of UHR-OCT for retinal imaging typically results in aberrations caused by the specific arrangement and imperfect curvatures of the cornea and lens. Additionally, diffraction represents a significant problem due to the limited pupil size, which, however, can be alleviated by pupil dilation. Thus, to optimize the OCT resolution and improve the imaging quality, aberrations should be removed [9,10]. Fernández *et al.* combined adaptive optics with UHR-OCT for imaging foveal cone photoreceptors to examine a larger number of retina features than those observed by conventional UHR-OCT systems [11]. Different types of light sources were

proposed for UHR-OCT systems, including multiple superluminescent diodes (SLDs) [12,13], mode-locked lasers (MLs) [14,15], and supercontinuum lasers (SCLs) [16,17]. A combination of multiple SLDs with different spectral regimes can broaden the effective spectrum range; however, the output power of the resulting light source remains limited. The results of previous studies demonstrated that MLs exhibited broadband spectra with ultrahigh axial resolutions. Werkmeister *et al.* also demonstrated an UHR-OCT system based on a broadband Ti: Sapphire laser with a center wavelength of 800 nm for *in vivo* imaging of human cornea. Attributed to a broad FWHM of 170 nm, the theoretical axial resolution can reach 1.2  $\mu\text{m}$  which could be potentially implemented for investigating physiology and pathophysiology of human cornea [18]. Furthermore, when a highly nonlinear fiber was pumped by a femtosecond laser such as a Ti:sapphire or Cr:forsterite, its spectral bandwidth could be significantly improved [19,20]. However, such solid-state lasers are expensive and bulky, which makes their use in clinical applications very difficult. Alternatively, pumping highly nonlinear fibers with a femtosecond fiber laser can reduce the laser size and facilitates its integration with the fiber-based OCT systems.

Recently, multiple research groups have proposed to use the ML-pumped SCL (ML-SCL) for UHR-OCT [21] and visible-light OCT (vis-OCT) [22] applications. Because the spectral range of ML-SCL typically spans from 400 to 2400 nm, the 800-nm and 1310-nm spectral components were individually utilized for the development of UHR-OCT systems in a previous study [23]. In contrast to the UHR-OCT systems in the near-infrared range, vis-OCT became an alternative solution to provide an ultrahigh axial resolution by utilization of the visible spectral range [24,25]. Due to the advantage of the specific absorption property in the visible range resulting from hemoglobin, vis-OCT can be used to determine hemoglobin oxygenation and to visualize microcirculation of the retina. In the previous reports, ML-SCLs were commonly implemented for vis-OCT by extracting the visible range for imaging [26,27]. However, due to the shorter wavelength used for imaging, the penetration depth of the vis-OCT system is much shallower than the OCT systems in the near-infrared range. Additionally, the permissible exposure power is lower in comparison to conventional OCT systems, making the imaging sensitivity poorer. Furthermore, ML-SCL has been also implemented in OCT angiography (OCTA) based on Doppler effect, decorrelation, spectral contrast, and optical microangiography (OMAG) [28–31]. In contrast, a Q-switch pumped SCL (QS-SCL) is difficult to realize in OCT due to the high level of its intrinsic noise. Although ML-SCLs have been widely used as the light source of UHR-OCT, the cost of a commercial ML-SCL system is approximately 8 times higher and its volume is approximately 6 times larger than the corresponding QS-SCL parameters. Therefore, QS-SCL could be an economic and compact solution for UHR-OCT. Maria *et al.* reported a 1.3- $\mu\text{m}$  QS-SCL-based UHR-OCT system and showed that the relative intensity noise (RIN) was the main noise source, which degraded its signal-to-noise ratio (SNR) [32]. However, the noise level of QS-SCLs is relatively high, and its output power is much lower than that of ML-SCLs. Therefore, the development of an efficient QS-SCL-based UHR-OCT/OCTA system remains a very challenging task.

In this study, we have utilized a commercial QS-SCL as the light source for constructing an UHR-OCT/OCTA apparatus operating in the 760-nm regime. The resulting spectral-domain OCT (SD-OCT) system with a specially designed spectrometer exhibits an effective spectral range of 635 – 875 nm. The SNR of this system is optimized by varying the exposure time of the line-scan camera. To further reduce the intrinsic RIN of the QS-SCL, a special algorithm is developed for OCT/OCTA imaging. Finally, the OCT/OCTA spectra of the developed UHR-OCT system are compared with the results obtained using a conventional FD-OCT setup.

## 2. Experimental setup

### 2.1. UHR-OCT system

Figure 1 shows the schematic diagram of the developed SD-UHR-OCT system. The commercial QS-SCL (SuperK compact, NKT Photonics, Demark) used in this setup provides an output power of 100 mW, spectral range of 450 – 2400 nm, and laser repetition rate of 20 kHz. The laser beam was collimated by the fiber collimator and sequentially passed through the notch filter (67-123, Edmund Optics, Singapore) and a dichroic mirror (DMSP1000, Thorlabs, New Jersey, USA) to cut off the spectral range corresponding to the pumping pulse with a wavelength of 1060 nm and reserve the spectral range of 600 – 900 nm for the interferometer. After passing the dichroic mirror, the optical power of the beam was 20 mW. Because the utilized spectral range covered approximately 240 nm with the center wavelength of 760 nm, it was difficult to find suitable fiber couplers. For this reason, a free-space UHR-OCT system was built in this study. In this system, the light beam passed through the dichroic mirror was incident on a polarization-independent beam splitter (BNPB-25.4B-45R-800, LAMBDA, New Jersey, USA) with a splitting ratio of 50:50 that divided it into the reference and sample arms, respectively. The sample arm was composed of a two-axis galvanometer (GVS002, Thorlabs, New Jersey, USA) and a scanning lens (LSM02BB, Thorlabs, New Jersey, USA), while the incident power on the sample was set to 4 mW. In the reference arm, a reflective mirror and a dispersion compensator (N-SF8, SCHOTT North America, New York, USA) were used. Subsequently, the interference beam was coupled into a single-mode fiber (SMF, P3-630A-FC-1, Thorlabs, New Jersey, USA) by a fiber coupling stage (KT110, Thorlabs, New Jersey, USA) and then recollimated again by another fiber coupling stage at the other end of the SMF to adjust the beam size incident on the input of the home-made spectrometer. The use of SMF can reduce the difficulty in the setup of spectrometer and improve the variation in the interference intensity due to the beam scanning in the sample arm. To study the feasibility of using the developed UHR-OCT/OCTA system for *in vivo* imaging, an existing swept-source OCT (SS-OCT) was implemented for comparison. The experimental setup of the 1060-nm SS-OCT system was described in a previous study, and the same scanning lens (LSM02BB, Thorlabs, New Jersey, USA) was used to focus the light beam on the sample [33]. The detailed specifications of both systems are shown in Table 1.

**Table 1. Specifications of UHR-OCT and SS-OCT**

	UHR-OCT	SS-OCT
Center wavelength	760 nm	1060 nm
FWHM	150 nm	90 nm
Measured axial resolution	2 $\mu\text{m}$	6 $\mu\text{m}$
Measured lateral resolution	10 $\mu\text{m}$	10 $\mu\text{m}$
A-scan rate	10 kHz	100 kHz
3 dB/6 dB sensitivity roll-off (OPL: optical path difference)	OPL@300 $\mu\text{m}$ /OPL@400 $\mu\text{m}$	OPL@400 $\mu\text{m}$ /OPL@500 $\mu\text{m}$
Frame rate	20 frames/s (500 A-scans/frame)	100 frames/s (1000 A-scans/frame)
Power on sample	4 mW	3 mW
Time (3D OCT)	25 s (500*500*2048)	10 s (1000*1000*1024)
Time (3D OCTA)	50 s (500*1000*2048)	20 s (1000*2000*1024)

### 2.2. Spectrometer

To design a spectrometer for the UHR-OCT system, the optical path was simulated using OpticStudio software (Zemax, Washington, USA), as shown in Fig. 2. The spectrometer consists

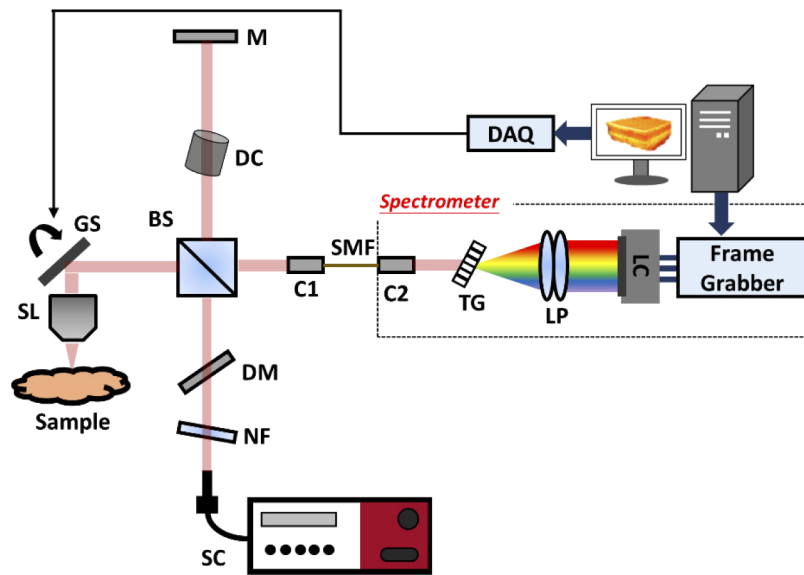


**Fig. 1.** A schematic of the developed spectral-domain UHR-OCT system with a commercial QS-SCL. SC: supercontinuum laser; NF: notch filter; DM: dichroic mirror; BS: beam splitter; DC: dispersion compensator; GS: galvanometer; SL: scanning lens; M: mirror; C1, C2: collimators; TG: transmission grating; LP: lens pair; LC: line-scan camera; and DAQ: data acquisition board.

of a transmission grating (1200 l/mm @ 840 nm, Wasatch Photonics, North Carolina, USA), a pair of achromatic lenses (AC508-200-B, Thorlabs, New Jersey, USA), and a line-scan camera (spL4096-140 km, Basler, German). Figure 2(a) depicts the corresponding positions of the optical components in the spectrometer. The beam emitted from the SMF was collimated by the fiber coupling stage onto the transmission grating with a period of 1200 lines/mm. After that, two achromatic lenses were used for the collimation of the dispersed beams into the line-scan camera. Figures 2(b)–(d) show the simulated spots with different sizes and wavelengths of 600, 750, and 900 nm, respectively, focused on the camera pixel grid. The simulated beam diameters are different at the wavelengths of 600, 750, and 900 nm, varying from 6 to 11  $\mu\text{m}$ . This was due to the aberration of the lens pair used in the spectrometer, which can be mitigated or suppressed in the future by using custom designed optic components. Finally, the line-scan camera was connected to a frame grabber through the Cameralink interface for data acquisition. To synchronize the image acquisition by the camera with the galvanometer, a data acquisition board (DAQ, PCIe-6229, National Instruments, Texas, USA) was utilized for the generation of analog signals. A pulse waveform was generated by the DAQ board as an external trigger to control the camera exposure time. Additionally, the two axes of the galvanometer were driven by a triangular wave and a step function produced by the DAQ board.

### 2.3. Spectral response

Although the developed UHR-OCT system is based on the free-space interferometer, the dispersion issue should be carefully addressed due to the unbalanced use of the optical components located between the reference and sample arms. For example, the scanning lens is part of the sample arm, but it causes a dispersion mismatch between both arms. In this study, a dispersion compensator is required for balancing the dispersion induced by the scanning lens. Additionally, the spectral responses of the optical components should be optimized to maximize the effective spectral

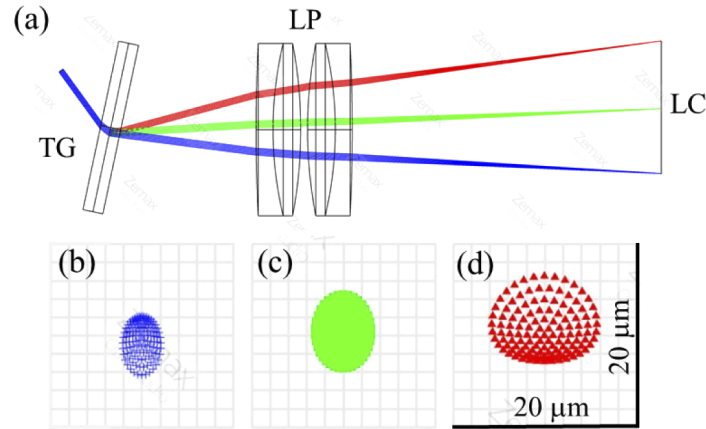


**Fig. 2.** (a) A schematic of the home-made spectrometer simulated by Zemax. The spectrometer consists of a transmission grating, two achromatic lens, and a line-scan camera. The detectable spectral range spanned from 600 nm to 900 nm. (b)–(d) The blue, green, and red spots represent the focused spots on the camera pixel grid with different sizes and wavelengths of 600, 750, and 900 nm, respectively. TG: transmission grating, LP: lens pair, and LC: line-scan camera.

range. In the setup depicted in Fig. 1, the scanning lens and galvanometer are used in the sample arm, and the dispersion compensator is inserted in the reference arm. Different dispersion compensators were utilized for comparison including a coated compensator (LSM02DC, Thorlabs, New Jersey, USA) and a compensator without coating (N-SF8, SCHOTT North America, USA). The thicknesses of both compensators were equal to 26 mm. The wavelength range of 500 – 900 nm was used for testing the spectral response of the UHR-OCT system after passing through the optical components of interferometer, and a commercial spectrometer (USB2000, Ocean Optics, UK) was employed to receive the output signal. Figure 3 displays the spectra individually recorded for the sample arm (blue line), reference arm (red line), and interference (black line) of both arms using the coated/uncoated dispersion compensators. It shows that the signal in the spectral range below 700 nm was significantly attenuated when the coated dispersion compensator was used, as indicated by the red line in Fig. 3(a). In the same figure, the intensity of the interference spectrum in the region below 700 nm was smaller than that of the corresponding spectrum in Fig. 3(b). Hence, the uncoated dispersion compensator was more suitable for the use in the developed UHR-OCT system due to its higher intensity of the interference signal.

#### 2.4. OCT angiography

In addition to the microstructural imaging with OCT, the developed system was also used for OCTA based on the estimation of its speckle variance. Repeated scanning was performed along the same transverse range to obtain two sequential two-dimensional (2D) OCT images, after which the variance of the backscattered speckle between these images  $SV(x, y)$  was estimated according to the following equation:

$$SV(x, y) = \frac{\{I_A(x, y) - \frac{1}{2}[I_A(x, y) + I_B(x, y)]\}^2 + \{I_B(x, y) - \frac{1}{2}[I_A(x, y) + I_B(x, y)]\}^2}{2} \quad (1)$$

where  $I_A$  and  $I_B$  represent the pixel intensities of the first and second frames, while  $x$  and  $y$  are the locations in the transverse and depth directions, respectively [34,35]. A threshold value was experimentally determined to reject the speckle noise and enhance the contributions from the



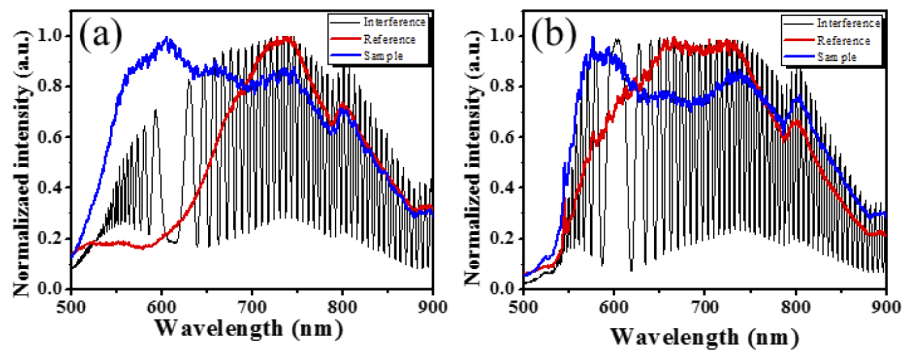


**Fig. 3.** Spectra recorded for the sample (blue lines) and reference (red lines) arms, and interference of the signals from both arms (black lines) using the (a) coated and (b) uncoated dispersion compensators.

vessels. However, the intrinsic noise of the QS-SCL should be removed before the estimation of the speckle variance.

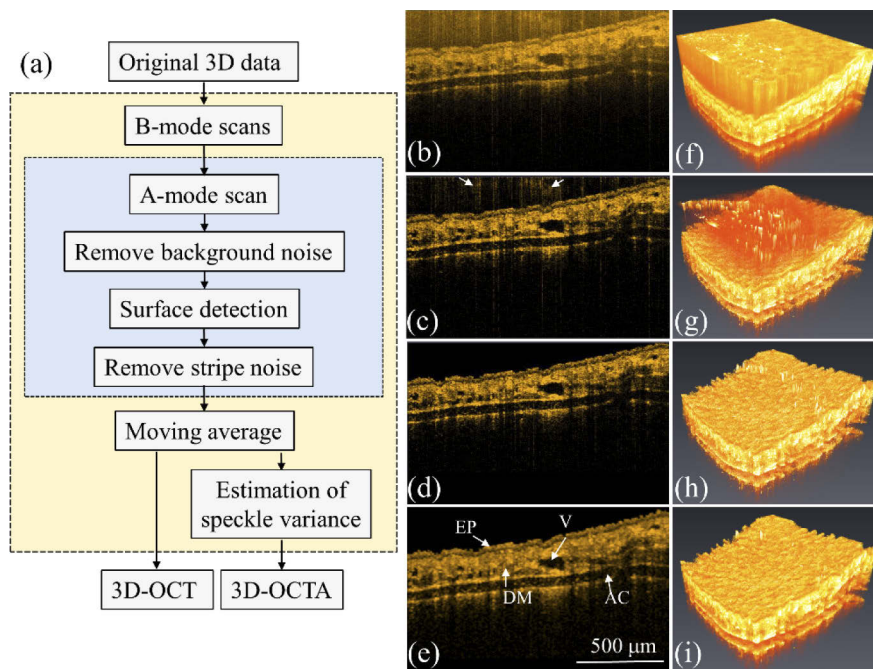


**Fig. 4.** (a) A flow chart of the processing algorithm for removing the intrinsic noise from the QS-SCL signal. 2D OCT images of the mouse ear skin obtained (b) before processing, (c) after the removal of the noise in the shallow depth range, (d) after the removal of the stripe-shaped noise, and (e) after the moving average calculation. (f)–(i) 3D OCT images corresponding to the images depicted in panels (b)–(e). EP: epidermis, DM: dermis, V: vessel, and AC: auricular cartilage.

### 2.5. Noise reduction

To reduce the intrinsic noise of the QS-SCL, an imaging process algorithm was developed. Figure 4(a) depicts the flow chart of the developed algorithm for the removal of the background noise. In this case, each B-scan consists of 500 A-scans covering the transverse distance of 1.5 mm, and each three-dimensional (3D) volume is composed of 500 B-scans. First, 500 A-scans were recorded when the sample arm was blocked and averaged to acquire the average background noise, which was subsequently subtracted from each A-scan. To remove the stripe-shaped noise, the sample surface was detected in each A-scan, and the noise intensity was averaged between the zero path and the sample surface. After that, the average noise intensity was again subtracted from the intensity of each pixel within individual A-scan below the sample surface to remove the stripe-shaped noise. Figures 4(b)–(e) show the 2D OCT images of the mouse ear skin obtained before processing (Fig. 4(b)), after the removal of the low-depth noise (Fig. 4(c)), after the removal of the stripe-shaped noise (Fig. 4(d)), and after the moving average calculation (Fig. 4(e)). Moreover, Figs. 4(f)–(i) display the 3D OCT images corresponding to the images depicted in Figs. 4(b)–(e). Although the noise in the shallow depth range could be easily removed, the stripe-shaped noise remained in the OCT images as indicated by the white arrows in Fig. 4(c). The latter also influenced the estimated speckle variance for OCTA. As shown in Fig. 4(d), the stripe-shaped noise can be effectively removed using the above-mentioned process. Finally, the moving average calculation was performed (Fig. 4(e)), in which the epidermis, dermis, vessels, and auricular cartilage could be clearly identified.

### 3. Evaluation of system performance

Although the spectral range spanning from 600 to 900 nm was used for the simulation of the optical path in the spectrometer, the spectral range at the CCD end only covered the region from 635 to 875 nm. This reduction in the spectral range likely resulted from the cut-off wavelength of the SMF and imperfect alignment of the optical components. Subsequently, the spectrometer was utilized for recording interference spectra (the corresponding experimental setup is shown in Fig. 1). Figure 5(a) shows the interference spectrum obtained by the line-scan camera that includes both the non-interference and interference terms, while Fig. 5(b) displays the interference spectrum obtained after the removal of the non-interference component. To perform the wavelength calibration prior to the Fourier transform, the interference spectrum was resampled using the method proposed in the previous study [36]. After wavelength calibration, the processed spectrum was filtered by a software-based Gaussian window and then, fast Fourier transform was performed to acquire the point spread function (PSF) as plotted in Fig. 5(c). Here, the axial resolution can be acquired by estimating the full-width at half-maximum of PSF as indicated by the black arrows [37]. Thus, the measured axial resolution approximately equals 2  $\mu\text{m}$  in air. Additionally, the SNR curves of the A-scans performed at various depths were recorded (see Fig. 5(d)). Each curve was averaged over 10 sequential A-scans conducted at the same depth. The data presented in Fig. 5(d) reveal that the noise floor was relatively high due to the RIN generated by the light source. Additionally, it can be found that the SNR decreased  $\sim 20$  dB at the depth of 1 mm. In our spectrometer, the spectral range covers from 635 to 875 nm, corresponding to a spectral resolution of 0.059 nm. The theoretical sensitivity roll-off is 18 dB when the optical path difference reaches 1 mm [38]. The difference in the theoretical and measured results may be resulted from imperfect resampling for wavelength calibration. The results of a previous study indicated that RIN of QS-SCL increased with the wavelength, but the RIN of the ML-SCL was wavelength-independent [39–41]. To further decrease the intrinsic RIN produced by the QS-SCL, the exposure time of the line-scan camera was optimized, and a new image-processing algorithm was developed.

Because the repetition rate of the utilized QS-SCL was 20 kHz, exposure times of 25, 50, and 100  $\mu\text{s}$  were used for the optimization of the system SNR. Figures 6(a)–(c) show the 2D OCT

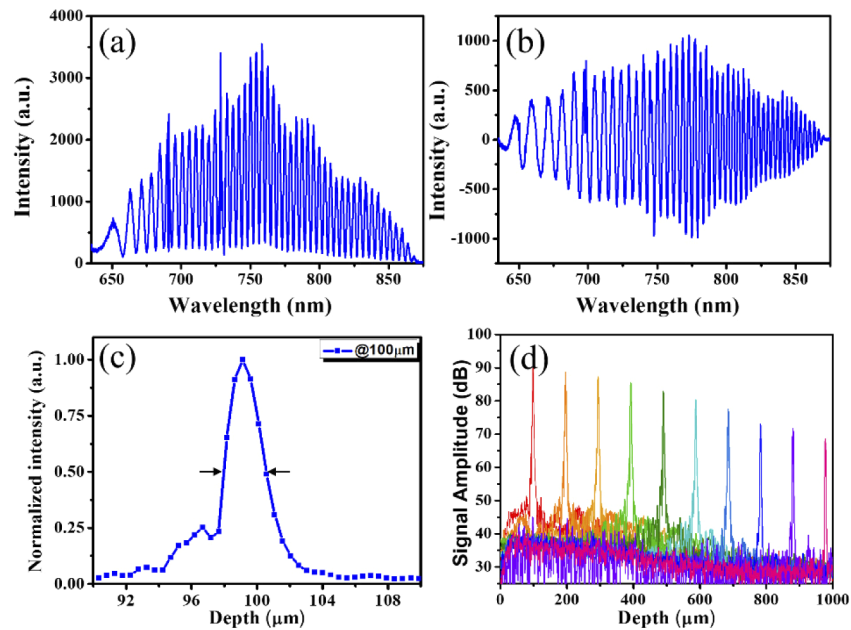


**Fig. 5.** Interference spectra obtained by the line-scan camera (a) before and (b) after the removal of the non-interference component. (c) PSF used for the evaluation of the axial resolution. (d) SNRs of the A-scans recorded at various depths.

images of the human skin obtained for the same volunteer at different exposure times. Here, each 2D OCT image was composed of 1000 A-scans. In Fig. 6(a), the dark stripes that degrade the imaging quality and increase the noise level are observed. Because the number of pulses generated by the QS-SCL during one B-scan was smaller than the total number of A-scans in each B-scan, some A-scans might be produced without pulses causing the appearance of black stripes in the corresponding OCT images. When the exposure time was increased to 50  $\mu\text{s}$ , which was equal to the pulse duration, the number of dark stripes was significantly reduced as shown in Fig. 6(b). In the latter case, the epidermis and dermis layers could be identified. Moreover, after further increasing the exposure time to 100  $\mu\text{s}$ , the skin structure became much clearer due to the increase in SNR. To determine the relationship between the sensitivity and exposure time, sensitivity roll-off curves were plotted at different depths and exposure times in Fig. 6(d). The obtained results revealed that the sensitivity at a depth of 100  $\mu\text{m}$  and exposure time of 100  $\mu\text{s}$  exceeded 90 dB; however, its value was reduced by around 20 dB at a depth of 1 mm. Furthermore, the sensitivity measured at an exposure time of 25  $\mu\text{s}$  was very small, making the *in vivo* imaging of biological tissues very difficult. Apart from the sensitivity measurements, the noise floor was also examined as a function of depth by averaging 1000 sequential A-scans, during which the sample arm was blocked. The obtained results illustrate that the noise floor decreased with increasing exposure time. Although the longer exposure times can effectively improve the SNR, they also decrease the imaging speed, owing to the existence of motion artifacts. Furthermore, a longer exposure time may lead to the loss of dynamic information related to the biological tissue (such as blood flow). Thus, the exposure time in the developed system was set to 100  $\mu\text{s}$  for *in vivo* imaging, which corresponded to an A-scan rate of 10 kHz. The resulting frame rate was 20 frames per second, and it took 25 s to acquire volumetric data.



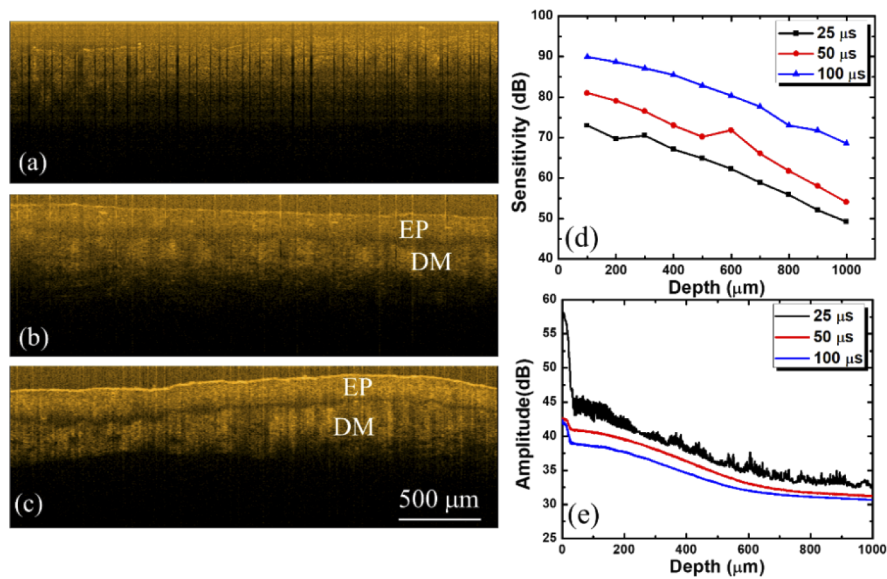


**Fig. 6.** 2D OCT images of the human skin obtained at exposure times of (a) 25, (b) 50, and (c) 100  $\mu$ s. EP and DM denote the epidermis and dermis layers, respectively. (d) Sensitivity roll-off curves plotted over a depth range of 1 mm at different exposure times. (e) Noise floors measured on the dB scale at exposure times of 25, 50, and 100  $\mu$ s. EP: epidermis and DM: dermis.

#### 4. Results

As shown in Figs. 6(d) and (e), the noise degraded the SNR, and a stronger noise was generated in the shallower depth range. Moreover, the high noise level increased the speckle variance between B-scans, making OCTA imaging difficult. The main noise can be divided into two types including the low-depth and stripe-shaped ones. In order to increase the detection sensitivity of UHR-OCT imaging, the return power in the reference arm was increased. However, such stripe-shaped noise may occur when stronger backscattered intensity caused by the sample resulted in the saturation of camera. Therefore, a processing algorithm for noise reduction was proposed as shown in Fig. 4(a). To investigate the feasibility of using the developed UHR-OCT for angiography at an imaging quality comparable with that of the conventional FD-OCT system, the former technique was implemented, and its results were compared with those of the existing SS-OCT system at a center wavelength of 1060 nm. The lateral resolutions of UHR-OCT and UHR-OCTA are approximately 10  $\mu$ m, respectively. The axial resolutions of UHR-OCT and SS-OCT are 2 and 6  $\mu$ m, and the incident powers on the sample of UHR-OCT and SS-OCT are 4 and 3 mW, respectively. For OCTA, the speckle variance between the two sequential OCT images was determined according to Eq. (1). The volumetric data of OCT/OCTA contained 500 B-scans, and each location was scanned twice to estimate the speckle variance (the same area of the mouse ear skin was individually scanned with both systems). For the animal experiments, mice (C57 wild-type, 7–8 weeks old, male) were anesthetized with a mixed aesthetic which was composed of oxygen and phenobarbital. The mouse was held on a customized mount, and the mouse ear was well fixed. The animal experiment conducted in this study was according to the approved protocol by the Laboratory Animal Center, Chang Gung University. First, the mouse ear was scanned by UHR-OCT, and it took 50 seconds for acquiring 3D OCT/OCTA imaging. Then, the mouse was quickly moved to the sample arm of SS-OCT, and the same skin area was scanned with SS-OCT to obtain 3D OCT/OCTA results. For SS-OCTA imaging, it took 20

seconds. After UHR-OCT imaging, no significant damage can be observed by the naked eye and from the OCT results.

Figures 7(a) and (b) show the representative 2D OCT images obtained by UHR-OCT and SS-OCT, which were selected from the corresponding 3D images at a close location. The magnified areas denoted by the yellow squares in Figs. 7(a) and (b) are depicted in Figs. 7(c) and (d), respectively. The white arrows indicate the vessel structures, and the magnified UHR-OCT image (Fig. 7(c)) displays a clear vessel boundary, which was blurred in Fig. 7(d). Additionally, Figs. 7(e) and (f) show the corresponding projection-view OCTA images obtained by the UHR-OCT and conventional SS-OCT systems, respectively. As compared with SS-OCT, the UHR-OCT image exhibits a significantly higher visible vessel density, which allows visualization of small vessels. Again, the areas indicated by the white and yellow squares are magnified in Figs. 7(g) and (h) for Fig. 7(e) and Figs. 7(i) and (j) for Fig. 7(f). These results illustrate that UHR-OCT can be used to visualize smaller vessels due to its higher resolution.

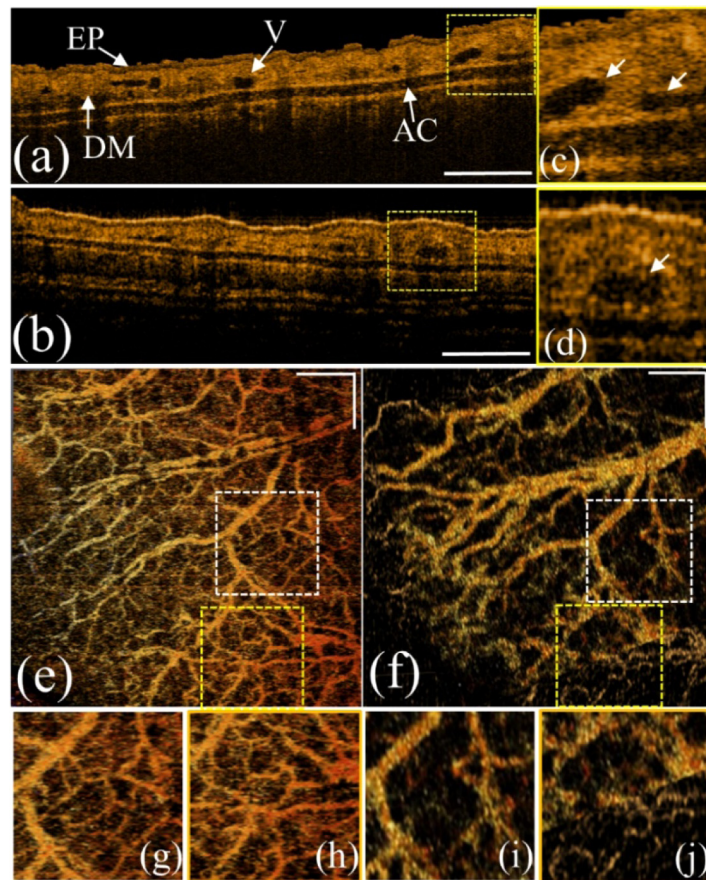


**Fig. 7.** 2D OCT images of the mouse ear skin obtained at a close location using the (a) UHR-OCT and (b) conventional SS-OCT systems. (c) and (d) Magnified OCT images of the areas indicated by the yellow squares in panels (a) and (b), respectively. Corresponding *en-face* projected OCTA images obtained by the (e) UHR-OCT and (f) conventional SS-OCT systems [33]. Magnified images of the areas indicated by the (g) white and (h) yellow squares in panel (e). Magnified images of the areas indicated by the (i) white and (j) yellow squares in panel (f). The scale bars represent a transverse distance of 250  $\mu\text{m}$ .

## 5. Discussion

Limited to the intrinsic noise of the QS-SCL, it is difficult to use QS-SCL for UHR-OCT/OCTA applications in the past. To understand the noise effect on the laser spectrum, the spectrum acquired by the UHR-OCT system with a blocked sample arm at an exposure time of 100  $\mu$ s is shown in Fig. 8(a). Its shape is not very smooth, and a strong intensity variation is observed due to the high RIN level. To further compare the RINs of ML-SCLs and QS-SCLs, a commercial ML-SCL (SuperK extreme EXW-12, NKT photonics) was used. The repetition rates of ML-SCL and QS-SCL are 78 MHz and 20 kHz, respectively. Because the light beam emitted from QS-SCL is well aligned with the free-space interferometer, the light sources cannot be easily exchanged without affecting the optics alignment. Therefore, the output spectra of both lasers are difficult to record by the developed OCT spectrometer. Instead, a commercial spectrometer (USB2000+, Ocean Optics) was utilized to cover the spectral range from 600 to 900 nm at an integration time of 1 ms. To estimate the RIN value, 100 time-series spectra were recorded for each laser. Its magnitude is defined as

$$\text{RIN} = \frac{\sigma_M(\lambda)}{M(\lambda)} \quad (2)$$

where  $\lambda$  is the wavelength.  $\sigma_M(\lambda)$  represents the standard deviation of the time-series powers at a given wavelength, and  $M(\lambda)$  is the mean of the time-series powers at a given wavelength [32]. Notably, the integration time was set to 1 ms, and each recorded spectrum consisted of 78000 laser pulses emitted from ML-SCL. In contrast, only 20 laser pulses emitted from QS-SCL were detected for each spectrum. Figure 8(b) plots the estimated RIN distributions of the ML-SCL and the QS-SCL as functions of wavelength, which show that the RINs of QS-SCL are higher than those of ML-SCL. Moreover, while the integration time of the commercial spectrometer was 1 ms, the exposure time of our QS-SCL-based OCT system was set to 100  $\mu$ s, suggesting that the RIN of the developed UHR-OCT setup should be much higher than the values depicted in Fig. 8(b).

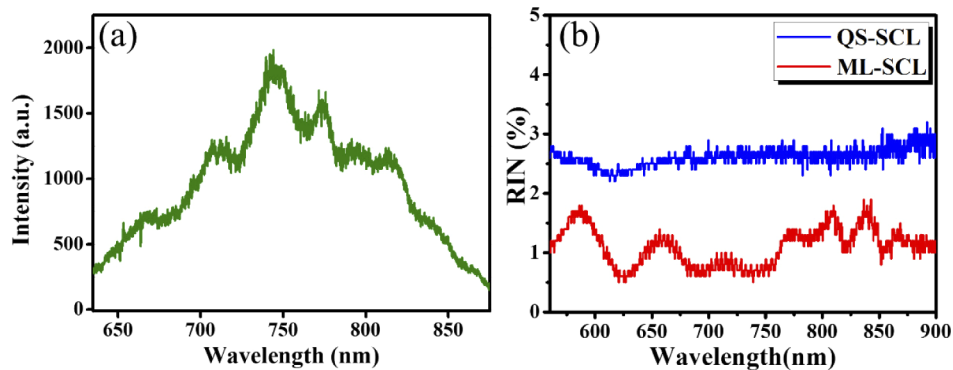


**Fig. 8.** (a) Output spectrum of the QS-SCL captured by the developed OCT spectrometer at an exposure time of 100  $\mu$ s. (b) Measured RINs of the QS-SCL used in the present study and the commercial ML-SCL (SuperK extreme EXW-12) as functions of wavelength. The integration time was set to 1 ms.

The measured sensitivities of the UHR-OCT and SS-OCT systems in this study were 91 dB and 106 dB, respectively. Additionally, the RINs of the QS-SCL laser and swept source used in this study were compared. To determine the RIN distribution of the proposed UHR-OCT system, the developed OCT spectrometer was used, and the exposure time varied between 50 and 100  $\mu$ s. One thousand spectra were recorded sequentially to estimate the RIN distribution for each exposure time. Figure 9(a) depicts the RIN distributions as functions of wavelength. It shows

that the smaller exposure times lead to higher RIN values. Moreover, the RIN of the 1060-nm SS-OCT system was estimated as well. For that purpose, a commercial NIR spectrometer (SW2540-050-NIRA, OtO Photonics, Taiwan) was used to directly obtain the spectra of the swept source, and 1000 sequential spectra were recorded at an integration time of 1 ms. Another 1000 sequential spectra were acquired by the balanced detector of the SS-OCT system when the sample arm was blocked. Because the A-scan rate of SS-OCT is 100 kHz, it takes approximately 10  $\mu$ s to acquire a full spectrum of the swept source. The RIN distributions estimated from the spectra obtained by the NIR spectrometer and balanced detector are shown in Fig. 9(b). Notably, the blue curve in Fig. 9(b) exhibits smaller RIN values because 100 full output spectra were received during one integration period. In the blue curve, the RIN magnitudes measured from 980 to 1025 nm are relatively large, which likely resulted from the lower responsivity of the NIR spectrometer. Hence, after comparing the green curve in Fig. 9(b) with the red curve in Fig. 9(a), it can be concluded that the RIN distribution of the swept source is located below that of QS-SCL.

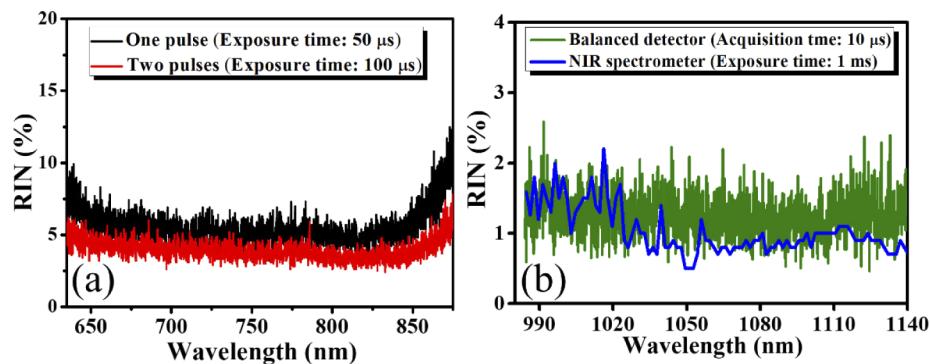


**Fig. 9.** (a) RIN distributions of the used QS-SCL captured by the developed OCT spectrometer when the exposure time was set to 50 and 100  $\mu$ s, respectively. (b) RIN distributions of the 1060-nm swept source measured from the commercial NIR spectrometer and the balanced detector of the SS-OCT system, respectively.

Additionally, the effect of RIN on OCTA was investigated by conducting phantom experiments. A capillary PE tube with an inner diameter of 300  $\mu$ m was connected to a syringe pump to provide a stable flow. After that, the PE tube was fixed on the sample stage and filled with soymilk. While the soymilk was pumped by the syringe pump, the same cross-sectional area of the PE tube was repeatedly scanned with UHR-OCT (an identical experiment was conducted for SS-OCT). Figure 10 shows the data obtained using the PE tube and the UHR-OCT and SS-OCT systems. Figures 10(a) and (b) present the UHR-OCT results obtained for the PE tube with a soymilk flow before and after performing the processing procedure outlined in Fig. 4(a), while Figs. 10(c) and (d) depict the corresponding SV images of Figs. 10(a) and (b). For comparison, the SS-OCT image of the PE tube with a soymilk flow and the corresponding SV image are shown in Figs. 10(e) and (f), respectively. Here, the yellow and white arrows indicate the PE tube and flowing soymilk, respectively. To quantitatively analyze the RIN effect on OCTA, a Weber contrast factor,  $C$ , was introduced. It was defined as  $C = (I - I_R) / I_R$ , where  $I$  and  $I_R$  represented the total intensities in the region of interest and reference region depicted by the yellow and red squares in Fig. 10, respectively. Table 2 lists the Weber contrast factors estimated for Fig. 10. Before conducting the processing procedure to remove the noise, the SV UHR-OCT data showed very little contrast; however, the contrast factor increased to 31.131 after noise elimination. As a result, the contrast factor of the processed UHR-OCT image became comparable with that of the SS-OCTA image.



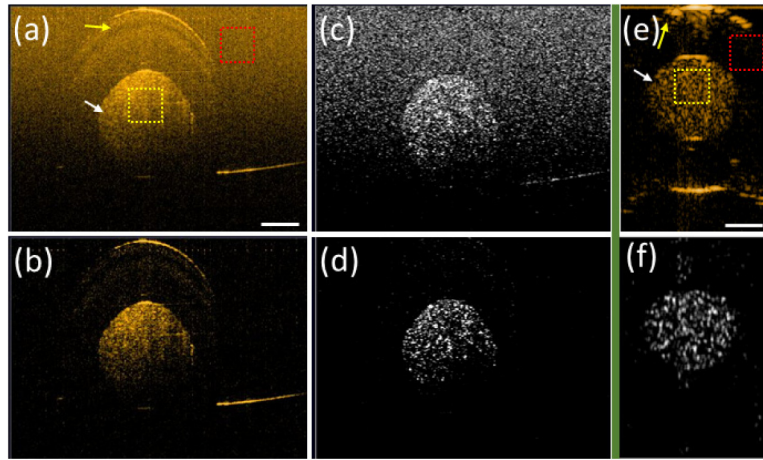


**Fig. 10.** OCT and OCTA images of the PE tube containing flowing soymilk obtained by the UHR-OCT and SS-OCT systems. (a), (b) UHR-OCT results obtained for the PE tube with a soymilk flow before and after performing the processing procedure. (c), (d) Corresponding SV images of (a) and (b). (e), (f) SS-OCT image of the PE tube with a soymilk flow and the corresponding SV image. The scalar bar denotes the length of 100  $\mu\text{m}$ .

**Table 2. Weber contrast factors estimated for Fig. 10**

	Original UHR image	Processed UHR image-	SS image
OCT	1.019	2.368	2.723
OCTA	0.285	31.131	32.952

In SD-OCT systems, the system sensitivity depends on the repetition rate of the light source, exposure time of the line-scan camera, and incident power on the sample. However, all these parameters are interrelated. When the exposure time was less than 50  $\mu\text{s}$ , it caused the formation of dark stripes in the OCT images shown in Fig. 6(a) because no laser pulses were detected by the line-scan camera during one exposure period. Additionally, it caused the larger intensity variation between A-scans when the exposure time was less than 100  $\mu\text{s}$  as shown in Fig. 6(b). Therefore, the exposure time was set to 100  $\mu\text{s}$  in our experiments, which corresponded to the duration of the two pulses received by the lines-can camera in one exposure period. Although the maximum repetition rate of the used QS-SCL system was 28 kHz, the laser was most stable during the operation at a repetition rate of 20 kHz. Because the exposure time and repetition rate were set to 100  $\mu\text{s}$  and 20 kHz, respectively, only the incident power on the sample and the reflected power from the reference arm were slightly adjusted to optimize the sensitivity for the reasons mentioned above. However, excessive incident power on the sample or excessive return power of the beam reflected from the reference arm caused intensity saturation of the camera at an exposure time of 100  $\mu\text{s}$ , which further degraded the imaging quality. In this study, 3D OCT imaging conducted at this A-scan rate (10 kHz) may result in the formation of motion artifacts. Moreover, OCTA is based on the estimation of the speckle variance between the two B-scans obtained for the same location, making OCTA imaging a challenging procedure. Although the number of motion artifacts can be decreased by reducing the A-scan number for each B-scan, the imaging quality is accordingly degraded. To effectively eliminate motion artifacts, different methods were used in previous studies, which could be also applicable to the developed UHR-OCT system [42,43].

Compared to conventional OCT systems, UHR-OCT is able to detect more specific and detailed features of biological tissue. However, the light sources commonly used for UHR-OCT such as



femtosecond lasers and ML-SCLs are difficult to be widely implemented for clinical applications because of the bulky size and the high cost. In contrast, commercially available QS-SCLs have the advantages of the smaller size and the much lower cost, making clinical applications in ophthalmology and dermatology feasible.

## 6. Summary

In this study, an UHR-OCT system based on the QS-SCL was developed for *in vivo* OCT/OCTA imaging. The spectral range from 635 to 875 nm was implemented for OCT, and a home-made spectrometer was designed to record a broadband interference spectrum. In addition, the spectral responses of the optical components were examined to maximize the effective spectral range and optimize the interference spectrum. The optimal exposure time of the line-scan camera equal to 100  $\mu$ s was determined to find a compromise between the system SNR and the scanning rate. To further improve the intrinsic noise level of the QS-SCL for OCTA, a processing algorithm was developed to reduce both the background noise in the shallow depth range and stripe-shaped noise resulting from the intensity saturation of the line-scan camera. After system optimization, the axial resolution was approximately 2  $\mu$ m, and the A-scan rate was as high as 10 kHz, which was acceptable for *in vivo* imaging. Finally, the developed system was implemented for both the OCT and OCTA *in vivo* imaging techniques. The obtained results confirmed that QS-SCLs could be successfully utilized for UHR-OCT/OCTA leading to significant reductions in the UHR-OCT cost and system size.

## Funding

Chang Gung Memorial Hospital (CMRPD2H0241); Ministry of Science and Technology, Taiwan (MOST 105-2221-E-182-016 MY3, MOST 107-2627-M-007 -005, MOST 107-2628-E-182-001-MY3); Ministry of Science and Technology, Taiwan (108-2636-E-002 -009).

## Acknowledgement

We appreciate the helpful discussions and suggestions from Prof. Linbo Liu at the Nanyang Technical University.

## Disclosures

The authors declare that there are no conflicts of interest related to this article.

## References

1. D. Huang, E. A. Swanson, C. P. Lin, J. S. Schuman, W. G. Stinson, W. Chang, M. R. Hee, T. Flotte, K. Gregory, and C. A. Puliafito, "Optical coherence tomography," *Science* **254**(5035), 1178–1181 (1991).
2. M. Siddiqui, A. S. Nam, S. Tozburun, N. Lippok, C. Blatter, and B. J. Vakoc, "High-speed optical coherence tomography by circular interferometric ranging," *Nat. Photonics* **12**(2), 111–116 (2018).
3. B. E. Bouma, S.-H. Yun, B. J. Vakoc, M. J. Suter, and G. J. Tearney, "Fourier-domain optical coherence tomography: recent advances toward clinical utility," *Curr. Opin. Biotechnol.* **20**(1), 111–118 (2009).
4. M. Stehouwer, F. Verbraak, H. de Vries, P. Kok, and T. Van Leeuwen, "Fourier domain optical coherence tomography integrated into a slit lamp; a novel technique combining anterior and posterior segment OCT," *Eye* **24**(6), 980–984 (2010).
5. M. Hermesmeier, S. Jeong, A. Yamamoto, X. Chen, U. Nagavarapu, C. L. Evans, and K. F. Chan, "Characterization of human cutaneous tissue autofluorescence: implications in topical drug delivery studies with fluorescence microscopy," *Biomed. Opt. Express* **9**(11), 5400–5418 (2018).
6. H. Mikami, J. Harmon, H. Kobayashi, S. Hamad, Y. Wang, O. Iwata, K. Suzuki, T. Ito, Y. Aisaka, and N. Kutsuna, "Ultrafast confocal fluorescence microscopy beyond the fluorescence lifetime limit," *Optica* **5**(2), 117–126 (2018).
7. N. Nishizawa, H. Kawagoe, M. Yamanaka, M. Matsushima, K. Mori, and T. Kawabe, "Wavelength dependence of ultrahigh-resolution optical coherence tomography using supercontinuum for biomedical imaging," *IEEE J. Sel. Top. Quantum Electron.* **25**(1), 1–15 (2019).
8. S. A. Boppart, B. E. Bouma, C. Pitris, J. F. Southern, M. E. Brezinski, and J. G. Fujimoto, "In vivo cellular optical coherence tomography imaging," *Nat. Med.* **4**(7), 861–865 (1998).

9. R. S. Jonnal, O. P. Kocaoglu, R. J. Zawadzki, Z. Liu, D. T. Miller, and J. S. Werner, "A review of adaptive optics optical coherence tomography: technical advances, scientific applications, and the future," *Invest. Ophthalmol. Visual Sci.* **57**(9), OCT51–OCT68 (2016).
10. M. Pircher and R. J. Zawadzki, "Review of adaptive optics OCT (AO-OCT): Principles and applications for retinal imaging [invited]," *Biomed. Opt. Express* **8**(5), 2536–2562 (2017).
11. E. J. Fernández, B. Hermann, B. Považay, A. Unterhuber, H. Sattmann, B. Hofer, P. K. Ahnelt, and W. Drexler, "Ultrahigh resolution optical coherence tomography and pancorrection for cellular imaging of the living human retina," *Opt. Express* **16**(15), 11083–11094 (2008).
12. T. H. Ko, D. C. Adler, J. G. Fujimoto, D. Mamedov, V. Prokhorov, V. Shidlovski, and S. Yakubovich, "Ultrahigh resolution optical coherence tomography imaging with a broadband superluminescent diode light source," *Opt. Express* **12**(10), 2112–2119 (2004).
13. R. G. Cucu, A. G. Podoleanu, J. A. Rogers, J. Pedro, and R. B. Rosen, "Combined confocal/en face T-scan-based ultrahigh-resolution optical coherence tomography in vivo retinal imaging," *Opt. Lett.* **31**(11), 1684–1686 (2006).
14. P. R. Herz, Y. Chen, A. D. Aguirre, J. G. Fujimoto, H. Mashimo, J. Schmitt, A. Koski, J. Goodnow, and C. Petersen, "Ultrahigh resolution optical biopsy with endoscopic optical coherence tomography," *Opt. Express* **12**(15), 3532–3542 (2004).
15. W. Drexler, U. Morgner, R. K. Ghanta, F. X. Kärtner, J. S. Schuman, and J. G. Fujimoto, "Ultrahigh-resolution ophthalmic optical coherence tomography," *Nat. Med.* **7**(4), 502–507 (2001).
16. G. Humbert, W. Wadsworth, S. Leon-Saval, J. Knight, T. Birks, P. S. J. Russell, M. Lederer, D. Kopf, K. Wiesauer, and E. Breuer, "Supercontinuum generation system for optical coherence tomography based on tapered photonic crystal fibre," *Opt. Express* **14**(4), 1596–1603 (2006).
17. H. Wang, C. P. Fleming, and A. M. Rollins, "Ultrahigh-resolution optical coherence tomography at 1.15  $\mu\text{m}$  using photonic crystal fiber with no zero-dispersion wavelengths," *Opt. Express* **15**(6), 3085–3092 (2007).
18. R. M. Werkmeister, S. Sapeta, D. Schmidl, G. Garhöfer, G. Schmidinger, V. A. dos Santos, G. C. Aschinger, I. Baumgartner, N. Pircher, F. Schwarzhans, A. Pantalon, H. Dua, and L. Schmetterer, "Ultrahigh-resolution OCT imaging of the human cornea," *Biomed. Opt. Express* **8**(2), 1221–1239 (2017).
19. L. Liu, J. A. Gardecki, S. K. Nadkarni, J. D. Toussaint, Y. Yagi, B. E. Bouma, and G. J. Tearney, "Imaging the subcellular structure of human coronary atherosclerosis using micro-optical coherence tomography," *Nat. Med.* **17**(8), 1010–1014 (2011).
20. N. Nishizawa, S. Ishida, M. Hirose, S. Sugiyama, T. Inoue, Y. Mori, K. Itoh, and H. Matsumura, "Three-dimensional, non-invasive, cross-sectional imaging of protein crystals using ultrahigh resolution optical coherence tomography," *Biomed. Opt. Express* **3**(4), 735–740 (2012).
21. N. M. Israelsen, M. Maria, M. Mogensen, S. Bojesen, M. Jensen, M. Haedersdal, A. Podoleanu, and O. Bang, "The value of ultrahigh resolution OCT in dermatology-delineating the dermo-epidermal junction, capillaries in the dermal papillae and vellus hairs," *Biomed. Opt. Express* **9**(5), 2240–2265 (2018).
22. X. Shu, L. J. Beckmann, and H. F. Zhang, "Visible-light optical coherence tomography: a review," *J. Biomed. Opt.* **22**(12), 121707 (2017).
23. A. Davis, O. Levecq, H. Azimani, D. Siret, and A. Dubois, "Simultaneous dual-band line-field confocal optical coherence tomography: application to skin imaging," *Biomed. Opt. Express* **10**(2), 694–706 (2019).
24. S. P. Chong, C. W. Merkle, C. Leahy, H. Radhakrishnan, and V. J. Srinivasan, "Quantitative microvascular hemoglobin mapping using visible light spectroscopic optical coherence tomography," *Biomed. Opt. Express* **6**(4), 1429–1450 (2015).
25. S. Pi, A. Camino, M. Zhang, W. Cepurna, G. Liu, D. Huang, J. Morrison, and Y. Jia, "Angiographic and structural imaging using high axial resolution fiber-based visible-light OCT," *Biomed. Opt. Express* **8**(10), 4595–4608 (2017).
26. S. Pi, A. Camino, W. Cepurna, X. Wei, M. Zhang, D. Huang, J. Morrison, and Y. Jia, "Automated spectroscopic retinal oximetry with visible-light optical coherence tomography," *Biomed. Opt. Express* **9**(5), 2056–2067 (2018).
27. C. Veenstra, W. Petersen, I. M. Vellekoop, W. Steenbergen, and N. Bosschaart, "Spatially confined quantification of bilirubin concentrations by spectroscopic visible-light optical coherence tomography," *Biomed. Opt. Express* **9**(8), 3581–3589 (2018).
28. S. Chen, X. Shu, J. Yi, A. A. Fawzi, and H. F. Zhang, "Dual-band optical coherence tomography using a single supercontinuum laser source," *J. Biomed. Opt.* **21**(6), 066013 (2016).
29. R. S. Shah, B. T. Soetikno, J. Yi, W. Liu, D. Skondra, H. F. Zhang, and A. A. Fawzi, "Visible-light optical coherence tomography angiography for monitoring laser-induced choroidal neovascularization in mice," *Invest. Ophthalmol. Visual Sci.* **57**(9), OCT86–OCT95 (2016).
30. J. A. Winkelmann, A. Eid, G. Spicer, L. M. Almassalha, T.-Q. Nguyen, and V. Backman, "Spectral contrast optical coherence tomography enables single-scan vessel imaging," *Light: Sci. Appl.* **8**(1), 7 (2019).
31. J.-P. Syu, W. Buddhakosai, S.-J. Chen, C.-C. Ke, S.-H. Chiou, and W.-C. Kuo, "Supercontinuum source-based multi-contrast optical coherence tomography for rat retina imaging," *Biomed. Opt. Express* **9**(12), 6132–6144 (2018).
32. M. Maria, I. B. Gonzalo, T. Feuchter, M. Denninger, P. M. Moselund, L. Leick, O. Bang, and A. Podoleanu, "Q-switch-pumped supercontinuum for ultra-high resolution optical coherence tomography," *Opt. Lett.* **42**(22), 4744–4747 (2017).

33. M.-T. Tsai, I.-C. Lee, Z.-F. Lee, H.-L. Liu, C.-C. Wang, Y.-C. Choia, H.-Y. Chou, and J.-D. Lee, "In vivo investigation of temporal effects and drug delivery induced by transdermal microneedles with optical coherence tomography," *Biomed. Opt. Express* **7**(5), 1865–1876 (2016).
34. A. Mariampillai, B. A. Standish, E. H. Moriyama, M. Khurana, N. R. Munce, M. K. Leung, J. Jiang, A. Cable, B. C. Wilson, and I. A. Vitkin, "Speckle variance detection of microvasculature using swept-source optical coherence tomography," *Opt. Lett.* **33**(13), 1530–1532 (2008).
35. M. S. Mahmud, D. W. Cadotte, B. Vuong, C. Sun, T. W. Luk, A. Mariampillai, and V. X. Yang, "Review of speckle and phase variance optical coherence tomography to visualize microvascular networks," *J. Biomed. Opt.* **18**(5), 050901 (2013).
36. Y. Yasuno, V. D. Madjarova, S. Makita, M. Akiba, A. Morosawa, C. Chong, T. Sakai, K.-P. Chan, M. Itoh, and T. Yatagai, "Three-dimensional and high-speed swept-source optical coherence tomography for in vivo investigation of human anterior eye segments," *Opt. Express* **13**(26), 10652–10664 (2005).
37. S. W. Lee, H. W. Jeong, B. M. Kim, Y. C. Ahn, W. Jung, and Z. P. Chen, "Optimization for Axial Resolution, Depth Range, and Sensitivity of Spectral Domain Optical Coherence Tomography at 1.3  $\mu\text{m}$ ," *J. Korean Phys. Soc.* **55**(6), 2354–2360 (2009).
38. N. Bosschaart, M. C. G. Aalders, T. G. van Leeuwen, and D. J. Faber, "Spectral domain detection in low-coherence spectroscopy Nienke," *Biomed. Opt. Express* **3**(9), 2263–2272 (2012).
39. W. J. Brown, S. Kim, and A. Wax, "Noise characterization of supercontinuum sources for low-coherence interferometry applications," *J. Opt. Soc. Am. A* **31**(12), 2703–2710 (2014).
40. W. Yuan, J. Mavadia-Shukla, J. Xi, W. Liang, X. Yu, S. Yu, and X. Li, "Optimal operational conditions for supercontinuum-based ultrahigh-resolution endoscopic OCT imaging," *Opt. Lett.* **41**(2), 250–253 (2016).
41. M. Jensen, I. B. Gonzalo, R. D. Engelholm, M. Maria, N. M. Israelsen, A. Podoleanu, and O. Bang, "Noise of supercontinuum sources in spectral domain optical coherence tomography," *J. Opt. Soc. Am. B* **36**(2), A154–A160 (2019).
42. D. W. Wei, A. J. Deegan, and R. K. Wang, "Automatic motion correction for in vivo human skin optical coherence tomography angiography through combined rigid and nonrigid registration," *J. Biomed. Opt.* **22**(6), 066013 (2017).
43. Y. Chen, Y.-J. Hong, S. Makita, and Y. Yasuno, "Eye-motion-corrected optical coherence tomography angiography using Lissajous scanning," *Biomed. Opt. Express* **9**(3), 1111–1129 (2018).